EY4667

Insights into the Multiscale Conductivity Mechanism of Marine Shales from Wufeng-Longmaxi Formation in the Southern Sichuan Basin of China

Huaimin Dong[1]; Xin Zeng[2]; Dalin Zhou[3]; Jinjiang Zhu[4]; Naser Golsanami[5]; Jianmeng Sun[6]; and Yihuai Zhang[7]

[1] Associate Professor, School of Geological Engineering and Geomatics, Chang'an University, Xi'an 710054, China (corresponding author). Email: sdsddhm@chd.edu.cn

[2] Dr, School of Geosciences, China University of Petroleum, Qingdao 266580, China. Email: zengx@upc.edu.cn

[3] Engineer, No. 12 Oil Production Plant, Changqing Oilfield Company, PetroChina, Xi'an 710200, China. Email: 1476195283@qq.com

[4] Engineer, No. 12 Oil Production Plant, Changqing Oilfield Company, PetroChina, Xi'an 710200, China. Email: 404898529@qq.com

[5] Associate Professor, College of Energy and Mining Engineering, Shandong University of Science and Technology, Qingdao 266590, China. Email: golsananami.n@gmail.com

[6] Professor, School of Geosciences, China University of Petroleum, Qingdao 266580, China. Email: sunjm@upc.edu.cn

[7] Lecturer, James Watt School of Engineering, University of Glasgow, Glasgow G12 8QQ, United Kingdom. Email: Yihuai.Zhang@glasgow.ac.uk

Abstract: Gas-bearing capacity is an important feature in the evaluation of the different properties of shale. The calculation of adsorbed gas and free gas content is the focus of the shale gas-bearing capacity evaluation, for which gas saturation is a key parameter. In the present study, the target area was the marine shales of the Wufeng-Longmaxi Formation in the Dingshan, Jiaoshiba, and Changning areas of the southern Sichuan Basin in China, while the purpose of the study was the more effective characterization of Langmuir's volume and Langmuir's pressure using well-logging data. The application of new well-logging technologies in the evaluation of shale gas-bearing capacity is seldom studied and the conventional sand-mudstone saturation models calculate the shale gas-bearing capacity with low accuracy. Therefore, this study systematically analysed the shale conductivity mechanism, which laid foundation for a new calculation model for shale gas saturation. The analysis results of the influencing factors of shale conductivity in the study area showed that the resistivity of shale in the interlayer is mainly affected by the low-resistivity thin layers, and the resistivity of shale in laminates is affected by clay minerals, pyrite, overmature conductive organic matter, and pore fluids. Moreover, this study further clarified the main controlling factors of the conductivity mechanism by implementing a multiscale analysis. Herein, on the meter-scale, the influence of low-resistivity thin layers on the shale resistivity was characterized based on a horizontal resistivity model; on the centimeter-scale, the influence of pore fluids on shale resistivity was investigated based on the rock electrical experiments; and on the nanometer-scale, the influence of clay minerals, pyrite, and organic materials on shale resistivity was examined based on digital rock technology and numerical simulation of the electrical properties. The results showed that the factors affecting the conductivity of the shale, from the strongest to the weakest, are conductive organic matter, low-resistivity thin layer, clay mineral, pore water and pyrite, respectively.

Keywords: Sichuan Basin; Marine shale; Multiscale; Conductive mechanism; Digital rock

Introduction

Shale gas is an unconventional type of natural gas that exists in organic-rich shale under free, adsorbed, and dissolved states (Curtis 2002; Dong et al. 2019a; Afagwu et al. 2022). Shale has low porosity, i.e., 0-15%, and extremely low permeability, i.e., <10 mD (Sun et al. 2015; Chen 2018; Memon et al. 2019), making it difficult for shale reservoirs to reach commercial production under natural conditions. However, the application of horizontal well technology and staged fracturing technology has appropriately resolved this issue (Liao et al. 2014; Wang 2014). China is rich in shale gas resources, with geological resources of 134×10^{12} m^3, and recoverable resources of 25.08×10^{12} m^3 (Fu 2014; Wang 2019; Zou et al. 2020a). Since 2009, the Ministry of Land and Resources of China, China National Petroleum Corporation, Sinopec, and China National Offshore Oil Corporation have successively carried out shale gas exploration and development work in the southern marine basin, the Ordos Basin, and the North China continental basin. As a result, technological breakthroughs have been made in two sets of shale formations: the Lower Cambrian Qiongzhusi Formation and the Upper Ordovician Wufeng Formation-Lower Silurian Longmaxi Formation in the southern marine basin (Huang et al. 2012; Nie et al. 2016, 2017; Zeng et al. 2020; Qiu et al. 2021; Li et al. 2022). For this reason, four national-level shale gas development and experimental zones have been successively established in Fuling, Zhaotong, Changning and Weiyuan (Li et al. 2009; Ma et al. 2018; Cui et al. 2019), forming a large-scale development capacity of shale gas with shallow marine facies of 3500 m. At present, the proven reserves of marine shale gas in China are 1.8×10^{12} m^3, and more than 700 shale gas wells have been put into production, with an output of about 145×10^8 m^3/a. Shale gas has become a crucial part of the increasing natural gas reserves and production in China (Li et al. 2018; Zou et al. 2020; Dai et al. 2021). The marine shale in the southern Sichuan Basin has the characteristics of continuous distribution with integrated source and reservoir, while the depositional environment is mainly a deep-water shelf with static water (Han et al. 2016; Wang et al. 2020). The structure and composition of shale are complex, where low-resistivity thin layers have developed in the vertical direction (Zhao et al. 2014; Li et al. 2016; Liu et al. 2022). In addition to quartz, feldspar, calcite and dolomite, the rock composition also includes conductive phases (pore water, clay minerals, pyrite, and overmature organic matter); the mineral composition is complex, and the framework minerals are conductive (Liu et al. 2019; Sun et al. 2022). The impact of different conductivity-controlling factors on resistivity is not a simple relationship, and the traditional argillaceous sandstone saturation model has poor accuracy in evaluating the gas saturation of marine shale in these areas (Liu et al. 2018; Hu et al. 2021). Therefore, it is necessary to analyse the influencing factors of the conductivity mechanism of shale, and develop a new evaluation method of gas saturation via electrical properties which does not suffer from the above-mentioned deficiencies.

Since the development of the Archie formula in 1942 (Kennedy 2001; Tan et al. 2014), the well-logging resistivity response has been widely used in the corresponding quantitative calculations of water saturation, which has greatly contributed to the development of well-logging formation evaluation (Glover et al. 2000; Hunt 2004; Hamamoto et al. 2010). In specific, the Archie formula introduced obtaining formation water saturation using rock resistivity and porosity values. The key to calculating fluid saturation by well-logging resistivity is the effective reflection of resistivity on pore fluids and an appropriate saturation calculation model (Abbasi et al. 2022). The original assumption in the application of the Archie formula was that only pore water conducts electricity in pure sandstone formations, while rock resistivity is only related to porosity and pore fluid saturation. However, for more complex sand-mudstone formations, except for pore water conductivity, clays with high irreducible water saturation and cation exchange ability also have a significant effect on resistivity (Golsanami et al. 2022). Therefore, it is necessary to correct the influence of clay when calculating the water saturation of sand-mudstone formations. Shale is a low-porosity and low-permeability reservoir with a small proportion of pores to rock volume (Xu et al. 2020). Therefore, the influence of pore fluids on rock resistivity is not as obvious as in conventional reservoirs, and the response of well-logging resistivity to shale gas content is weak. Due to the dual constraints of skeleton and pore fluids, the factors affecting the conductivity of shale are much more complicated than those of conventional sand-mudstone formations. During the process of exploration and development of shale formations in the Wufeng-Longmaxi Formation in the southern Sichuan Basin, it was found that there were great differences in shale resistivity, for only an insignificant difference in the depositional environment and lithology. At the same time, there were high-resistivity areas of greater than 100 Ω·m, medium-resistivity areas of 5-100 Ω·m, and low-resistivity areas of less than 5 Ω·m (Zeng et al. 2020; Sun et al. 2022). The great difference in resistivity of the same formation makes it difficult to accurately evaluate shale gas saturation with resistivity logging. Due to the many factors affecting shale resistivity and the complex conductivity mechanism, there is no effective method to calculate gas saturation based on resistivity. Sand-mudstone formation saturation models, such as Archie, Simandoux and Total-Shale, are widely used to calculate gas saturation in shale, but the calculation results of gas saturation are quite different from core analysis saturation and gas test productivity (Golsanami et al. 2020). Considering the limitations of the sand-mudstone saturation model and the difficulty in obtaining the saturation model parameters from rock electrical experiments, non-electrical methods such as the organic carbon ratio method (Shi et al. 2015), the neutron density intersection method (Zhang et al. 2017), and the nuclear magnetic resonance (NMR) method can be adopted to calculate shale gas saturation. These approaches have certain effectiveness, but still suffer from the following problems:

i. The organic carbon ratio method considers that the shale with high organic carbon content also has high gas saturation, which equates gas generation capacity with gas-bearing capacity while ignoring the effects of physical properties and preservation conditions on the gas-bearing capacity of shale.

ii. When the shale is gas-bearing, both the density and neutron logging value decrease. The neutron density intersection method uses the reverse overlap of the neutron density curve to calculate the gas saturation. However, organic matter and natural gas have the same effect on density logging. Therefore, the neutron logging value is easily affected by the water-bearing clay minerals, and the neutron density intersection method cannot fully reflect the gas-bearing properties of shale.

iii. The NMR method to evaluate shale gas saturation assumes that the organic pores and free fluid pores are completely gas-bearing, that the clay pores and capillary pores are water-bearing, while the gas saturation is calculated according to the difference in fluid properties of different pore types. However, the transverse relaxation time (T_2) values of different types of pores often overlap, and it is difficult to distinguish different types of pores by using the T_2 cut-off value, and the NMR method has great error in calculating the gas saturation.

In conclusion, although non-resistivity methods have achieved certain results in calculating shale gas saturation, these methods are often empirical and limited. Nevertheless, since the publication of the Archie formula, the evaluation of rock saturation through well-logging resistivity has become an important and indispensable part of well-logging formation evaluation.

To deepen the application of resistivity logging in shale gas saturation evaluation, and improve the utilization efficiency of well-logging data, this research takes the marine shale of the Wufeng-Longmaxi Formation in the Jiaoshiba, Dingshan, and Changning areas of the southern Sichuan Basin as the research targets. Also, this study uses well-logging data and core analysis data of multiple wells to analyse the factors affecting marine shale resistivity, while investigating the shale conductivity at different scales. That is, based on the horizontal resistivity calculation model, rock electrical experiments, and digital rock electrical numerical simulation, the conductivity law of shale at meter-scale, centimeter-scale, and nanometer-scale is considered respectively. Combined with the analysis of factors influencing conductivity and the study of conductivity laws, the main controlling factors of shale conductivity were determined. The purpose of this research was to establish a conductivity model and a gas saturation evaluation method suitable for marine shale in the study area, which could also be appropriately modified for other marine shales. This provides technical support for the calculation of free gas content in marine shale and the accurate interpretation of gas shale logging data.

Geological background

Shale gas accumulation is characterized by self-generation and self-storage, diverse occurrence states, and complex accumulation mechanisms (Chalmers and Bustin 2007; Zhang et al. 2012). Therefore, the continuity, gas-bearing, and fractability of marine shale gas reservoirs in southern China have become the most basic evaluation contents in shale gas geological research, exploration, and development in this area. Also, they are generally controlled by the sedimentary environment and the process of sedimentation. The Sichuan Basin, located in the northwest of the Yangtze Craton, is a tectonically stable sedimentary basin (Dai et al. 2016; Dong et al. 2018a), as shown in Fig. 1. Structurally, the basin margin is bounded by a series of deep and steep faults in both the northeast and northwest directions (Wang et al. 2018), which has always been an important oil and gas production area in China. Moreover, it is also a major area of shale gas development currently in China, due to its complete stratigraphic and marine stratigraphic development. The Dingshan area is located in the southeast fault-fold belt of the Sichuan Basin, which is influenced by the Huayingshan fault, Qiyueshan fault, and Zunyi fault, while the structural form is a nose-shaped fault anticline. The Jiaoshiba area is located in the Fuling District of the Chongqing Municipality, which is a deep continental shelf on the western side of the Yangtze Block, and its structural condition is relatively stable (Wang et al. 2019). The Changning area is located in the south of the

Changning County and on the north of the Junlian County. The majority of the gas fields are located on the southern slope of the Changning anticline, and generally have a saddle-shaped structure. The overlying strata dip of the Wufeng-Longmaxi Formation is weak and is buried in a depth of 2300-3200 m (Sun et al. 2022).

The shale of the Silurian Wufeng-Longmaxi Formation is the main stratum for shale gas exploration at this stage, due to its wide distribution, large sedimentary thickness, and rich organic matter (Li et al. 2015; He et al. 2022). Wufeng-Longmaxi Formation can be divided into three lithological sections from bottom to top, i.e., the deep grey-black siliceous shale and calcareous shale of shelf facies at the bottom; grey-dark carbonaceous graptolite shale and silty shale of deepwater and semi-deepwater shelf facies at the middle; and the grey-green, light grey, and grey clayey shale of semi-deepwater and shallow water shelf facies at the top (Feng et al. 2016; Zhao et al. 2016). Furthermore, the bottom is the main shale gas-producing layer, and the top is the regional sealing layer. The organic-rich black shale developed in the Wufeng-Longmaxi Formation in the Dingshan, Jiaoshiba, and Changning areas of southern Sichuan is the main target area for the present study.

Samples, experiments, and methods

Samples

To investigate the different electrical characteristics, marine shale samples were collected from 11 wells of the Wufeng-Longmaxi Formation in the study area for experiments. The location of the wells is shown in Fig. 1. The samples in the Dingshan area are initiated with DY and DYS, while the samples in the Jiaoshiba area are initiated with JY and TY. For the experiments, seven and six samples were collected from the Dingshan and Jiaoshiba areas, respectively. Besides, a sample was collected from the Changning area. Before the experiments, all samples were well-preserved in order to avoid the effects of weathering or oxidation. The total organic carbon (TOC) contents measured by the geochemical analysis experiments showed that the TOC contents ranged from 1.19 to 6.59%, with an average of 3.71%. In addition, the contents of minerals measured by the X-ray diffraction experiments showed that quartz, feldspar, clay minerals, calcite, and pyrite were the main compositions of the shale matrix. The quartz content was between 23.9 and 76.6%, with an average of 44.89%. The clay mineral content was in the range of 12.4 to 56.1%, with a mean value of 33.29%. Among the clay minerals, illite and illite/smectite mixed layer were the dominant minerals, and the average contents were 57.27% and 35.69% respectively. Other mineral contents in the shale matrix were not high, and the average values for feldspar, calcite, and pyrite were 5.01%, 13.52%, and 3.00%, respectively. The selected representative samples to illustrate the basic rock parameters are shown in Table 1.

Meter-scalehorizontal resistivity calculation methods

In well-logging interpretation, the formation with a thickness less than the instrument resolution is usually called a thin layer, and the laterolog vertical resolution is about one meter (Ni et al. 2018; Xia et al. 2001; Wei et al. 2021). Due to the limitation of the instrument's vertical resolution, the laterolog resistivity is inevitably affected by the low-resistivity thin layer, and it is difficult to reflect the true resistivity of the shale. The resistivity of shale developed in thin layers has obvious anisotropy, and the horizontal resistivity is different from the vertical resistivity. The horizontal resistivity indicates the parallel conduction of thin layers with high and low resistivity, while the vertical resistivity refers to the series conduction of thin layers with high and low resistivity. The ratio of parallel and series conduction is related to the layer's thickness (Zeng et al. 2020; Sun et al. 2022).

$$R_h = \left(\frac{f_L}{R_L} + \frac{f_H}{R_H} \right)^{-1} \tag{1}$$

$$R_v = f_L R_L + f_H R_H \tag{2}$$

$$f_L = \frac{h_L}{h_H + h_L} \tag{3}$$

$$f_H = \frac{h_H}{h_H + h_L} \tag{4}$$

$$f_H + f_L = 1 \tag{5}$$

$$\lambda = R_v / R_h \tag{6}$$

where R_h and R_v are the horizontal and vertical resistivities; R_L and R_H are the resistivities of the low-resistivity layer and high-resistivity layer; f_L and f_H are the proportion of the low-resistivity layer and high-resistivity layer; h_L and h_H are the thickness of the low-resistivity layer and high-resistivity layer; while λ is the ratio of vertical resistivity to horizontal resistivity, i.e., coefficient of resistivity anisotropy. This coefficient mainly reflects the conductivity difference of shale in horizontal and vertical directions, which can be obtained by dividing the vertical resistivity by the horizontal resistivity.

Centimeter-scale rock electrical experiments

The centimeter-scale conductivity law was studied by rock electrical experiments on standard shale samples with a diameter of 2.54 cm. The original shale had low water saturation and no liquid hydrocarbon in the pores; therefore, washing oil and salt before conducting the rock electrical experiment was not necessary. The experimental process is as follows:

i. The shale samples were dried at 100 °C for 48 hours, during which free pore water, capillary pore water, and clay intergranular water can be removed. After drying, the length, diameter, mass, resistivity, and NMR T_2 spectrum of the rock samples were measured, and the resistivity of the shale was calculated by using the length, diameter, and resistivity of the rock.

ii. After the shale was dried, the porosity and permeability were measured by gas measurement, and the gas source was helium.

iii. The equivalent NaCl salinity of formation water in adjacent layers of shale formation in the study area was as high as 72925 mg/L. In order to reduce the influence of formation water salinity on resistivity and highlight the influence of water saturation, NaCl solution with a salinity of 30000 ppm was implemented as the solution for saturating the samples.

iv. The shale samples were placed into the saturating solution to self-absorb water for 5 minutes. After the self-absorption, the moisture on the surface was removed with the use of moistened absorbent paper. Then, the samples were placed into a dryer with constant temperature and humidity for 4 hours, to make the pore water of the shale distribute evenly. After the completion of resting, the samples were weighted, and then the resistivity was measured by a digital bridge. During the measurement, 1 mm thick conductive rubber was added between the core and the probe to make the resistivity data stable and reliable. Herein, the pressure inside the sample holder was about 0.2 MPa, and excessive clamping could easily produce fractures. After the resistivity measurement, the samples were wrapped with a thin plastic wrap to measure the NMR T_2 spectrum and observe the distribution of water inside the pore space. The purpose of wrapping the shale with a plastic cover was to prevent water evaporation, as the NMR measurement environment was kept at a constant temperature of 30 ℃ and the measurement time was rather long.

v. The samples were put into the solution to self-absorb water for 15 minutes, 30 minutes, 1 hour, 2 hours, 4 hours, 8 hours, 32 hours, and 64 hours, respectively. After the water absorption was completed at different time lengths, the process of resting in step (iv) and measuring the weight, resistivity, and NMR responses of each sample was repeated. As a result, the resistivity and NMR T_2 spectra of shale under different water absorption times were obtained.

vi. After 64 hours of self-absorption of the shale samples, it was difficult to increase saturation through capillary self-suction. Therefore, the method of vacuum-pumping and pressurized saturation was adopted to saturate all samples with water for 24 hours at 7 MPa, 14 MPa, and 21 MPa, respectively. Rubber bands were used to bind the shale in the process of saturation, which not only can prevent the shale from breaking due to water saturation pressure, but also can prevent water from entering shale pores. After pressurized saturation, step (iv) was repeated for measuring the weight, resistivity, and NMR measurements under different saturation pressures.

vii. Combined with the variation of NMR T_2 spectrum and resistivity of shale during the saturation process, the relationship between shale resistivity and pore fluid saturation was analysed.

In the process of rock self-absorption and pressurized water saturation, pore water saturation can be calculated based on the change of rock mass, or by using the NMR experiment, i.e., the area under the NMR T_2 spectrum (Connolly et al. 2019; Zeng et al. 2020). The formulas for calculating water saturation based on mass change (weighing method) and T_2 spectral area change of NMR are shown in Eq. (7) and Eq. (8):

$$S_w = \frac{(m_i - m_{dry}) / \rho_w}{V \times \phi} \quad (7)$$

where, S_w is water saturation, %; m_i is the shale mass after the i-th saturation, g; m_{dry} is the mass of dried shale, g; ρ_w is the density of the configured aqueous solution, g/cm^3; V is the rock volume, cm^3; and Φ is the rock gas porosity, %.

$$S_w = \frac{S_i - S_{dry}}{S_{saturated} - S_{dry}} \quad (8)$$

where, S_i is the NMR T_2 spectral area of the rock after the i-th saturation; S_{dry} is the NMR T_2 spectrum area after drying; $S_{saturated}$ is the NMR T_2 spectrum area after pressurized saturation of 21 MPa, which assumed that shale is completely saturated after pressurized saturation of 21 MPa, and pore water saturation is 100%.

In the present study, the experimental equipment implemented for weighing the samples, for the resistivity measurement and the NMR measurement were a balance with a precision of 0.001 g, the TH2810B LCR digital bridge, and the Niumag MesoMR23 NMR instrument, respectively. The main frequency of the NMR instrument was 21 MHz, the waiting time (TW) was 6 s, the echo spacing (TE) was 0.1 ms, the number of scans (NS) was 32, the number of echoes (NECH) was 4000, and the measurement sequence was the Carr-Purcell-Meiboom-Gill (CPMG) pulse sequence.

Digital rock electrical numerical simulation

Shale porosity is usually dominated by nanoscale pores (Guo et al. 2020). The resolution of an ordinary X-ray CT scanner is usually at the micron level; hence, it is difficult to capture the distribution of nanoscale pores and throats using ordinary CT machines (Gou et al. 2018, Dong et al. 2018b). Focused Ion Beam Scanning Electron Microscopy (FIB-SEM) enables the reconstruction of shale 3D spatial distribution at the nanoscale through continuous cutting and imaging of the sample. Thus, this technology is used to characterize the microstructure of shale. According to the difference of grey values of different rock components, pores, clay, clastic minerals, organic matter, and pyrite, they can be segmented and extracted, which not only provides the possibility of displaying their 3D spatial distribution, but also can be used to simulate electrical or other petrophysical properties. The processing process is as follows. Firstly, the rock was scanned by a multi-resolution scanning electron microscope to determine the best scanning resolution and area (Fig. 2). The SEM images of JY8-3 at the resolution of 25 μm/pixel, 0.625 μm/pixel, and 0.225 μm/pixel are shown in Fig. 2a, Fig. 2c, and Fig. 2e, while the SEM images of DY1-2 at the resolution of 1.0 μm/pixel, 0.1 μm/pixel, and 0.036 μm/pixel are shown in Fig. 2b, Fig. 2d, and Fig. 2f. The samples were prepared as blocks, and the surface of each block was polished with an argon ion beam to produce a smooth surface. Each sample was coated with a 10 nm thick layer of gold to improve conductivity. Then, FIB-SEM was used to slice the rock and take hundreds of high-resolution images with a fixed field of view. These images were cropped to ensure that the same target area on the rock was locked accurately, and the accurate cropped images were further grey processed to reflect the pores and skeleton correctly. Next, Gaussian filtering was performed on the original images to achieve the purpose of eliminating noise and improving the signal-to-noise ratio of the image. Finally, these processed 2D images were superimposed into 3D images to obtain 3D digital rocks of the shale samples, i.e., 3D digital shale samples.

Based on the 3D digital shale, the effective resistivity of the rock was calculated using the finite element method (for more information on the finite element equations and solution methods, please refer to e.g., Sasaki 1999; Keehm et al. 2011; Liu et al. 2009; Dong et al. 2019; 2022). Based on the variational principle, an electric field was applied at any two ends of the 3D digital rock. The energy of the entire rock was determined by the final voltage distribution on each pixel point, and the total energy of the 3D digital rock could be expressed as a quadratic polynomial of the voltage at all nodes. Taking the minimum value of the total energy of the system, the conjugate gradient method was used to determine the voltage values of all nodes, and by calculating such parameters as the average current and total energy in the 3D digital rock, its effective resistivity could be obtained.

Results and discussion

Meter-scale conductivity law

During the depositional period at the bottom of the Wufeng-Longmaxi Formation, there were many large-scale volcanic eruptions that formed the potassium-rich bentonite through sedimentation, diagenesis, and alteration in the marine alkaline environment. Drilling cores have proven the existence of more than 20 layers of potassium bentonite in the stratum at the bottom of the Wufeng-Longmaxi Formation, with a thickness of 1 ~2 cm for a single layer, and up to 30 cm for an individual layer. Bentonite is a kind of clay rock mainly composed of illite and illite/smectite mixed layers (Guo et al. 2016). The bentonite layer, rich in clay minerals, is a low-resistivity thin layer. Such layers appear as a dark band on the FMI images (Fig. 3). The vertical resolution of the deep lateral resistivity is 0.9 m, which is affected by the low-resistivity and thickness of the thin layer within the longitudinal resolution range. The shale resistivity has obvious anisotropy, and the horizontal resistivity is significantly smaller than the vertical resistivity (Klein and Martin 1997). According to the laterologprinciple controlled by the shield electrode and the loop electrode, the deep laterolog current flows into the formation in an approximately horizontal shape, and the logging resistivity is more influenced by the horizontal resistivity, resulting in a lower resistivity value. This ultimately leads to higher water saturation calculated by the deep laterolog resistivity, and consequently an underestimation of the gas-bearing capacity of the shale. When the low-resistivity thin layer of shale is not developed and the electrical imaging log shows the blocky characteristics, the blocky shale has a high resistivity due to the discontinuous conduction path and the rock's hindering effect on the electric current.

In order to analyse the influence of low-resistivity thin layers on shale resistivity, the horizontal and vertical resistivities of shale were calculated within a 1 m window length. The resistivities of the high-resistivity layer and low-resistivity layer were set as 20 Ω·m and 5.0 Ω·m, while the ratio of the low-resistivity layer was set as 0.5. The variation of horizontal and vertical resistivities with the resistivity of the low-resistivity layer was simulated, as shown in Fig. 4.

The simulation results showed that the vertical resistivity is mainly controlled by the resistivity of the high-resistivity layer, when the proportion of the low-resistivity layer remains unchanged. The lower the resistivity of the low-resistivity layer, the greater the difference between the horizontal and vertical resistivities, and the greater the error in calculating the gas saturation using the horizontal resistivity. Under the condition that the resistivity of the low-resistivity layer remains unchanged, the smaller the proportion of the low-resistivity layer is, the closer the horizontal and vertical resistivities are to the resistivity of the high-resistivity layer. On the contrary, the greater the proportion of the low-resistivity layer is, the closer the horizontal and vertical resistivities are to the low-resistivity layer. When the ratio of the low-resistivity layer is equal to 0.5, the anisotropy coefficient is the largest, and the difference between horizontal resistivity and vertical resistivity is more significant.

Centimeter-scale conductivity law

Seven original shale samples, named JY5-2, JY5-5, JY8-3, DY1-2, DY2-3, DY3-1, and DYS1-1, were collected from the drill cores to carry out the rock electrical experiment. Before the rock electrical experiment was carried out, the mineral components and geochemical information of the samples were measured. The basic information of the shale samples is shown in Table.1. Due to the strong brittleness and well-developed lamination of shale, diamond wire cutting was used instead of drilling to cut out the shale samples into standard samples. At this stage, the following facts were taken into consideration.

i. The NMR T_2 spectrum of the core is the true reflection of the pore fluid contents. Therefore, the relationship between the resistivity index and the water saturation of shale was established based on the water saturation calculated through the NMR method. The variation of the T_2 NMR spectrum and resistivity index with water saturation of shale samples (Fig. 5) shows that the shale still has a certain NMR signal after drying, which is not because the shale is not thoroughly dried, but because of the hydrogen content of clay crystal water and organic matter in the shale.

ii. During the self-absorption process of shale, water is under the combined action of pore capillary force, surface hydrogen bonding force of clay minerals, van der Waals force on the surface of pore fractures, and surface hydration force between clay mineral lattices (Gao et al. 2013). After 5 minutes of water absorption, a large amount of water enters the pore space (Sun et al. 2021). The water content of large pores and small pores increases at the same time, but the water content of small pores increases more. After that, with the increase of water absorption time, the water saturation of shale further increases, and the T_2 spectrum amplitude and area gradually increase as well. Due to the larger capillary pressure in small pores, water mainly enters into small pores at first, and then enters large pores. The left boundary of the NMR T_2 spectrum remains unchanged, and the right boundary gradually shifts to the right.

iii. The capillary suction in the large pores of shale is insufficient, and the increase in self-absorption water is small. After pressurized saturation, water is injected into the large pores through the combined force of capillary self-suction and pressurized saturation. After pressurized saturation, the NMR T_2 spectrum of shale has little change, indicating that the shale pores are mainly small pores, and high-water saturation can be achieved by capillary self-suction.

iv. The variation of the shale resistivity index with water saturation conforms to Archie's formula. The lithology coefficient of the three shale blocks is about 1.0, and the saturation exponents are 1.23, 1.001, and 1.384, respectively. Yet, the saturation exponent of pure sandstone dominated by intergranular pores is generally around 2.0. Compared with pure sandstone, the saturation exponent of shale is smaller, and the effect of water saturation on shale resistivity is not obvious. However, previous researchers also obtained similar results when they carried out lithoelectric experiments on shale and tight sandstone (You et al. 2016). It is believed that the reasons for the small shale saturation exponent are as follows:

i. Clay and conductive minerals have a great influence on shale resistivity, which covers up the influence of pore fluid on resistivity, resulting in the phenomenon that shale resistivity does not significantly change with the variation of water saturation. The higher the clay content, the larger the cation exchange capacity and the smaller the saturation exponent (Sun and Chu 1994; Fan et al. 1997);

ii. Although the water augmentation method can establish a series of water saturations, the change process of pore fluid saturation is inconsistent with the actual accumulation conditions. When the non-wetting phase (gas) is displaced by the wetting phase (water), the saturation exponent is low (Liu et al. 1998; Sun et al. 2006);

iii. The inorganic pores of shale have strong hydrophilicity, while the organic pores still have certain hydrophilicity, resulting in the overall hydrophilicity of shale pores, and the hydrophilic rock saturation exponent is generally less than 2.

In summary, the centimeter-scale rock electrical experiment results show that the variation of the shale resistivity with water saturation conforms to the Archie formula, but the saturation exponent is less than 2, and the effect of water saturation on the shale resistivity is weaker than that of sandstone with medium-high porosity and permeability, which is mainly affected by conductive minerals in the shale’s structure, clay minerals, and the overall hydrophilicity of rocks.

Nanometer-scale conductivity law

Taking DYS1-3 and MY1-2 samples as examples, the FIB-SEM scanning results are shown in Fig. 6.

The three-dimensional reconstructed image of the shale microstructure is shown in Fig. 7, which used 500 continuously captured SEM images, and the overall size of the reconstructed image is 6.827 μm × 5 μm × 5.893 μm. The dark-black components are pores, the grey-black components are organic matter, the white shiny components are pyrite, the dark grey components are clay, and the light grey components are inorganic detrital minerals such as quartz and feldspar.

According to the difference in grey values of different shale components, organic matter, pores, pyrite, and other components can be separated and extracted to display their distribution forms in three-dimensional space, as shown in Fig. 8.

The finite element method is used to simulate the influence of rock components on shale resistivity via the constructed 3D digital rock models. The resistivity of clay, conductive organic matter, and pyrite were set as 5.0 Ω·m, 0.02 Ω·m, and 0.002 Ω·m, respectively. The resistivity of non-conductive organic matter and pore fluid were 0 Ω·m. Hence, only the influence of framework minerals was simulated.

The numerical simulation results revealed that the conductivity mechanism of shale is complex, and the additional conductivity of conductive minerals has a great influence on its electrical properties, whether or not the organic matter that conducts electricity has a great influence on the shale resistivity. When the organic matter conducts electricity (Fig. 9a), it acts as a resistivity-reducing component in the rock.

With the increase of the organic matter content, the conduction path of the rock increases, and the resistivity decreases. When the organic matter is not conductive (Fig. 9b), it causes an increase in resistivity, and the resistivity of rock increases with the increase of organic matter content.

Pyrite is a common metallic mineral in shale, which has strong electrical conductivity, and it is generally distributed in strips or in dispersed form. In this study, pyrite had a dispersed distribution in digital rock models. By randomly placing pyrite into the skeleton, 3D digital shale samples with different contents of pyrite were constructed, and the finite element method was used to simulate the variation of the shale resistivity. Fig. 10a shows that, with the increase of pyrite content, some local current paths gradually form in the rock, resulting in a rapid decline in resistivity. Besides, as the pyrite content continues to increase, the local current path continues to increase, but there is still no penetration path in the rock, and the resistivity decline gradually slows down. When the pyrite content is greater than 16%, the resistivity decreases to a very low value, and tends to remain fairly stable. In addition, viewed from different directions of the rock, with the increase of pyrite content, the resistivity in the Z direction decreases negative-exponentially, and the resistivity in the X and Y directions decreases relatively smoothly, almost linearly. This is due to the layered joints of shale flakes, resulting in a large difference in shale resistivity in the lateral and longitudinal directions, where the lateral conductivity is parallel, and the longitudinal conductivity is in series. Clay is the main component of shale, and it is necessary to study the influence of its content on the electrical properties of shale. The simulation results (Fig.10b) show that the resistivity of shale decreases gradually with the increase of clay content. This is because clay acts as an additional conductive phase in shale. With the increase of clay content, the conductive path of shale shortens, the conductive cross-section increases, and the resistivity decreases.

Fig. 11 shows the influence of different components on resistivity. Whether the organic matter is conductive or not has the greatest influence on the conductivity of the digital shale, and both clay and pyrite have certain additional conductivity. Among these, with the change of content, clay has a greater influence on electrical conductivity, while pyrite has no significant impact on the resistivity of digital rock due to its dispersed distribution. A comprehensive analysis of the influencing factors of shale's conductivity at various scales revealed that the ranking regarding influence, from strong to weak, is determined as conductive organic matter, low-resistivity thin layer, clay minerals, pore water, and pyrite, respectively. It should be noted that the influence of different factors on shale resistivity is mainly obtained by comparing the resistivity changes caused by the unit content changes of different influencing factors.

Conclusions

The marine shales of the Wufeng-Longmaxi Formation in the Dingshan, Jiaoshiba, and Changning areas of the southern Sichuan Basin were the targets of the present research study. Given the existence of low-resistivity shale in the study area, the traditional sand-mudstone saturation model has low accuracy in calculating the shale gas saturation in this area. Hence, the influencing factors and conductivity mechanism of shale are systematically analysed by joint usage of the meter-scale horizontal resistivity calculation model, the centimeter-scale rock electrical experiments, and the nanometer-scale digital rock electrical numerical simulation. After all, the following conclusions could be drawn.

When the ratio of low-resistivity layers remains unchanged, the vertical resistivity is mainly controlled by the resistivity of high-resistivity layers. The lower the resistivity of low-resistivity layers, the greater the difference between horizontal resistivity and vertical resistivity, therefore, the greater the error of calculating gas saturation by using horizontal resistivity would be. Besides, when the resistivity of the low-resistivity layer remains unchanged, the smaller the proportion of the low-resistivity layer is, the closer the horizontal and vertical resistivities are to the resistivity of the high-resistivity layer; the larger the proportion of the low-resistivity layer is, the closer the horizontal and vertical resistivities are to the resistivity of the low-resistivity layer.

The variation of the shale resistivity with water saturation follows Archie's formula, but the saturation exponent is less than 2. The influence of water saturation on the shale resistivity is weaker than that of sandstone with medium-high porosity and permeability, which is mainly affected by conductive skeleton minerals, clay minerals, and the overall hydrophilicity of the rock.

When organic matter conducts electricity, it acts as a resistivity reduction component in the rock. With the increase of organic matter content, the conductive path of rock increases, and the resistivity of rock decreases accordingly. When organic matter is not conductive, the resistivity of rock increases with the increase of organic matter content. Besides, with the increase of pyrite content, some local current paths gradually form in the rock, which results in the rapid decrease of rock resistivity. If the pyrite content continues to increase, the local current path also continues to increase, but there is still no penetration path in the core, and the resistivity gradually decreases. The resistivity of shale decreases with the increase of clay content. This is because clay is an additional conductive phase of shale, and with the increase of clay content, the conductive path of shale shortens, the conductive cross-section increases, and the resistivity decreases.

The analysis of the factors affecting shale's electrical properties, and the research results of the multiscale conductivity mechanism, show that the influencing factors of shale's electrical properties, from strong to weak, are conductive organic matter, low-resistivity thin layer, clay minerals, pore water and pyrite, respectively. This lays a solid foundation for the construction of a shale conduction model, in which the high- and low-resistivity layers conduct parallel conduction, while the high-resistivity layer contains organic matter, pyrite, clay, and pore water for mixed conduction.

Data Availability Statement

All data that support the findings of this study are available from the corresponding author upon reasonable request.

Acknowledgments

This work was supported by the Youth Program of National Natural Science Foundation of China (Grant No. 42204105), the China Postdoctoral Science Foundation (Grant No. 2021M700525), the National Natural Science Foundation of Shaanxi Province of China (Grant No. 2022JQ-293), the High-level Innovation and

Entrepreneurship Talent Program of Qinchuangyuan (Grant No. QCYRCXM-2022-24), the National Natural Science Foundation of Shandong Province of China (Grant No. ZR2022QD080).

Author Contributions: **Huaimin Dong:** investigation, writing-original draft preparation and funding acquisition; **Xin Zeng:** investigation, petrophysical experiment and methodology; **Dalin Zhou**: Data curation and images processing; **Jinjiang Zhu:** Visualization and data processing; **Naser Golsanami:** supervision, writing-reviewing and editing; language editing; **Jianmeng Sun:** conceptualization, supervision and funding acquisition; **Yihuai Zhang:** writing-reviewing and editing.

References

Abbasi, G. R., A. Al-Yaseri, F. U. R. Awan, A. Isah, A. Keshavarz, and S. Iglauer. 2021. "Effect of rock wettability on the electric resistivity of hydrate formations: An experimental investigation." Energy & Fuels, 35(24): 20037-20045.

Afagwu, C., M. A. Mahmoud, S. Alafnan, and S. Patil. 2022. "Multiscale storage and transport modeling in unconventional shale gas: A review". Journal of Petroleum Science and Engineering, 208: 109518.

Chalmers, G. R. L., and R. M. Bustin. 2007. "The organic matter distribution and methane capacity of the Lower Cretaceous strata of Northeastern British Columbia, Canada." International Journal of Coal Geology, 70: 223-239.

Chen, Q. 2018. "Characteristics of shale gas in Middle Permian Tongziyan Formation in Fujian Province." Coal Geology and Exploration, 46(4): 79-85.

Chen, Z., Y. Song, Z. Li, S. Liu, Y. Li, G. Liu, W. Yang, Q. Wang, Y. Yang, and F. Gao. 2019. "The occurrence characteristics and removal mechanism of residual water in marine shales: A case study of Wufeng-Longmaxi shale in Changning-Weiyuan area, Sichuan basin." Fuel, 253: 1056-1070.

Connolly, P. R. J., W. Yan, D. Zhang, M. Mahmoud, M. Verrall, M. Lebedev, S. Iglauer, P. J. Metaxas, E. F. May, and K. L. Johns. 2019. "Simulation and experimental measurements of internal magnetic field gradients and NMR transverse relaxation times (T2) in sandstone rocks." Journal of Petroleum and Science and Engineering, 175: 985-997.

Cui, H., F. Liang, C. Ma, N. Zhong, Y. Sha, and W. Ma. 2019. "Pore evolution characteristics of Chinese marine shale in the thermal simulation experiment and the enlightenment for gas shale evaluation in South China." Geoscience Journal, 23: 595-602.

Curtis, J. B. 2002. "Fractured shale-gas systems." AAPG Bulletin, 86(11): 1921-1938.

Dai, J., C. Zou, D. Dong, Y. Ni, W. Wu, D. Gong, Y. Wang, S. Huang, J. Huang, C. Fang, and D. Liu. 2016. "Geochemical characteristics of marine and terrestrial shale gas in China." Marine and Petroleum Geology, 76: 444-463.

Dai, J., Y. Ni, D. Dong, S. Qin, G. Zhu, S. Huang, C. Yu, D. Gong, F. Hong, Y. Zhang, Z. Yan, Q. Liu, X. Wu, and Z. Feng. 2021. "2021-2025 is a period of great development of China's natural gas industry: Suggestions on the exploration and development of natural gas during the 14th five-year plan in China." Journal of Natural Gas Geoscience, 6(4): 183-197.

Dong, D., Z. Shi, S. Sun, C. Guo, C. Zhang, W. Guo, Q. Guan, M. Zhang, S. Jiang, L. Zhang, C. Ma, J. Wu, N. Li, and Y. Chang. 2018a. "Factors controlling microfractures in black shale: A case study of Ordovician Wufeng Formation-Silurian Longmaxi Formation in Shuanghe Profile, Changning area, Sichuan Basin, SW China." Petroleum Exploration and Development, 45(5): 763-774.

Dong, H., J. Sun, N. Golsanami, L. Cui, L. Jiang, G. Yan, W. Yan, and Y. Li. 2018b. "A method to construct high-precision complex pore digital rock." Journal of Geophysics and Engineering, 15(6): 2695-2703.

Dong, H., J. Sun, J. Zhu, Z. Lin, L. Cui, W. Yan, and Z. Xiong. 2019a. "Quantitative characterization and characteristic analysis of pore structure of shale-gas reservoir in the Sichuan Basin, China." Interpretation, 7(4): 23-32.

Dong, H., J. Sun, J. Zhu, L. Liu, Z. Lin, N. Golsanami, L. Cui, and W. Yan. 2019b. "Developing a new hydrate saturation calculation model for hydrate-bearing sediments". Fuel, 248: 27-37.

Dong, H., J. Sun, M. Arif, Y. Zhang, W. Yan, S. Iglauer, and N. Golsanami. 2022. “Digital rock-based investigation of conductivity mechanism in low-resistivity gas hydrate reservoirs: Insights from the Muli area’s gas hydrates.” Journal of Petroleum Science and Engineering, 218: 110988.

Fan, Y., S. Deng, and C. Zhou. 1997. “On the parameters of Archie formula for shaly sand with low salinity.” Well-logging Technology, 3: 46-50.

Feng, Z., D. Liu, S. Huang, W. Wu, D. Dong, W. Peng, and W. Han. 2016. “Carbon isotopic composition of shale gas in the Silurian Longmaxi Formation of the Changning area, Sichuan Basin.” Petroleum Exploration and Development, 43(5): 705-713.

Fu, C. 2014. “China’s shale gas and shale oil resources: Opportunities and challenges.” Energy Exploration and Exploitation, 32(5): 759-769.

Gao, S., Z. Hu, W. Guo, L. Zuo, and R. Shen. 2013. “Water absorption characteristics of gas shale and the fracturing fluid flowback capacity.” Natural Gas Industry, 33(12): 71-76.

Golsanami, N., M. N. Jayasuriya, W. Yan, S. G. Fernando, X. Liu, L. Cui, X. Zhang, Q. Yasin, H. Dong, and X. Dong. 2022. “Characterizing clay textures and their impact on the reservoir using deep learning and Lattice-Boltzmann simulation applied to SEM images.” Energy, 240: 122599.

Golsanami, N., E. Bakhshi, W. Yan, H. Dong, E. Barzgar, G. Zhang, and S. Mahbaz. 2020. “Relationships between the geomechanical parameters and Archie’s coefficients of fractured carbonate reservoirs: a new insight.” Energy Sources, Part A: Recovery, Utilization, and Environmental Effects, 1-25.

Glover, P. W. J., M. J. Hole, and J. Pous. 2000. “A modified Archie’s law for two conducting phases.” Earth and Planetary Science Letters, 180(3-4): 369-383.

Gou, Q., S. Xu, F. Hao, Y. Lu, A. Zhang, Y. Wang, X. Cheng, and J. Qing. 2018. “Characterization method of shale pore structure based on nano-CT: A case study of Well JY-1.” 39(11): 1253-1261.

Guo, X., D. Hu, X. Wei, and Y. Li. 2016. “Main controlling factors on shale fractures and their influences on production capacity in Jiaoshiba area, the Sichuan Basin.”

Oil and Gas Geology, 37(6): 799-808.

Guo, J., D. Zhao, X. Liang, K. Yang, H. Li, and D. Long. 2020. “Quantitative characterization of shale nanopore structure: A case study of Wufeng Formation in southeastern Sichuan.” Lithologic Reservoirs, 32(5): 113-121.

Hamamoto, S., P. Moldrup, K. Kawamoto, and T. Komatsu. 2010. “Excluded-volume expansion of Archie’s law for gas and solute diffusivities and electrical and thermal conductivities in variably saturated porous media.” Water Resources Research, 46(6): 6514.

Han, C., Z. Jiang, M. Han, M. Wu, and W. Lin. 2016. “The lithofacies and reservoir characteristics of the Upper Ordovician and Lower Silurian black shale in the Southern Sichuan Basin and its periphery, China.” Marine and Petroleum Geology, 75: 181-191.

He, S., Q. Qin, H. Li, and S. Zhao. 2022. “Geological characteristics of deep shale gas in the Silurian Longmaxi Formation in the Southern Sichuan Basin, China.” Frontiers in Earth Science, 9: 818155.

Hu, Z., R. Wang, Z. Liu, G. Liu, D. Feng, Z. Yang, and P. Wang. 2021. “Source-reservoir characteristics and coupling evaluations for the lower Jurassic lacustrine shale gas reservoir in the Sichuan Basin.” Earth Science Frontiers, 28(1): 261-272.

Huang, J., C. Zou, J. Li, D. Dong, S. Wang, S. Wang, and K. Cheng. 2012. “Shale gas generation and potential of the Lower Cambrian Qiongzhusi Formation in the Southern Sichuan Basin, China.” Petroleum Exploration and Development, 39(1): 75-81.

Hunt, A. G. 2004. “Continuum percolation theory and Archie’s law”. Geophysical Research Letters, 31(19): L19503.

Keehm, Y., T. Mukerji, and A. Nur. 2001. “Computational rock physics at the pore scale: Transport properties and diagenesis in realistic pore geometries.” The Leading Edge, 2001, 20(2): 180-18.

Kennedy, W. D. 2001. “Calculating water saturation in electrically anisotropic media.” Petrophysics, 42(2): 118-136.

Li, D., J. Li, S. Wang, and X. Li. 2009. “Analysis of controls on gas shale reservoirs.”

Natural Gas Industry, 5: 22-26.

Li, D., R. Li, Z. Zhu, X. Wu, J. Cheng, F. Liu, and B. Zhao. 2017. “Origin of organic matter and paleo-sedimentary environment reconstruction of the Triassic oil shale in Tongchuan City, southern Ordos Basin (China).” Fuel, 208: 223-235.

Li, J., X. Wang, G. Wei, W. Yang, Z. Xie, Z. Li, J. Guo, Y. Wang, W. Ma, J. Li, and A. Sheng. 2018. “New progress in basic natural gas geological theories and future exploration targets in China.” Natural Gas Industry, 38(4): 37-45.

Li, S., J. Yang, B. Jiang, Q. Jiang, X. Wei, and L. Yang. 2022. “Analysis of physical properties and influencing factors of Longmaxi shale in Sichuan Basin.” Journal of Energy Engineering, 148(6):

Li, X., Y. Wang, J. Zhang, M. Guo, P. Zhao, H. Xu, J. Yang, and F. Wang. 2016. “Pore characteristics of shale gas reservoirs from the Lower Paleozoic in the southern Sichuan Basin, China.” Journal of Natural Gas Geoscience, 1(3): 195-202.

Li, Y., H. Lv, Y. Zhang, X. Zhang, D. Shao, J. Yan, and T. Zhang. 2015. “U-Mo covariation in marine shales of Wufeng-Longmaxi Formations in Sichuan Basin, China and its implication for identification of watermass restriction.” Geochimica, 44(2): 109-116.

Liao, Q., J. Ni, Q. Chen, H. Chen, and W. Huang. 2014. “The application of shale gas well test technology in multi-staged fracturing horizontal well.” Science Technology and Engineering, 14(14): 171-174.

Liu, J., J. Sheng, and W. Huang. 2019. “Experimental investigation of microscopic mechanisms of surfactant-enhanced spontaneous imbibition in shale cores.” Energy & Fuels, 33(8): 7188-7199.

Liu, R., W. Zhou, H. Xu, Q. Zhou, K. Jiang, F. Shang, W. Gao, W. Song, D. Liu, H. Zhao, and X. Zhao. 2022. “Impact of minerals and sealing systems on the pore characteristics of the Qiongzhusi formation shale in the Southern Sichuan Basin.” ACS Omega, 7(18): 15821-15840.

Liu, X., J. Sun, and H. Wang. 2009. “Numerical simulation of rock electrical properties based on digital cores.” Applied Geophysics, 6(1): 1-7.

Liu, X., Y. Lu, Y. Lu, L. Chen, Y. Ma, and C. Wang. 2018. “The application of geostatistical inversion in shale lithofacies prediction: A case study of the Lower Silurian Longmaxi marine shale in Fuling area in the southeast Sichuan Basin, China.” Marine Geophysical Research, 39: 421-439.

Liu, Z., T. Liu, and J. Yan. 1998. “Analysis of the effects of temperature, pressure, shaliness, wettability and experimental approach on Archie equation.” Well-logging Technology, 4: 7-12.

Ma, Y., X. Cai, and P. Zhao. 2018. “China’s shale gas exploration and development: Understanding and practice.” Petroleum Exploration and Development, 45(4): 561-574.

Memon, A., A. Li, W. Han, and W. Tian. 2019. “Effect of gas adsorption-induced pore radius and effective stress on shale gas permeability in slip flow: New insights.” Open Geosciences, 11(1): 948-960.

Ni, X., G. Xu, S. Xu, J. Feng, K. Bie, and D. Liu. 2018. “Analysis of influencing factors of polarization angle of dual laterolog apparent resistivity curves at stratigraphic interface.” Petroleum Geology and Recovery Efficiency, 25(2): 15-19.

Nie, H., and Z. Jin. 2016. “Source rock and cap rock controls on the Upper Ordovician Wufeng Formation-Lower Silurian Longmaxi Formation shale gas accumulation in the Sichuan Basin and its peripheral areas.” Acta Geological Sinica-English Edition, 90(3): 1059-1060.

Nie, H., Z. Jin, X. Ma, Z. Liu, T. Lin, and Z. Yang. 2017. “Graptolites zone and sedimentary characteristics of Upper Ordovician Wufeng Formation-Lower Silurian Longmaxi Formation in Sichuan Basin and its adjacent areas.” Acta Petrolei Sinica, 38(2): 160-174.

Qiu, N., W. Liu, X. Fu, W. Li, Q. Xu, and C. Zhu. 2021. “Maturity evolution of Lower Cambrian Qiongzhusi Formation shale of the Sichuan Basin.” Marine and Petroleum Geology, 128: 105061.

Sasaki, Y. 1999. “3D resistivity inversion using the finite-element method.” Geophysics, 11: 1839-1848.

Shi, W., C. Zhang, Z. Zhang, S. Xie, Y. Shi, and Y. Ren. 2015. “Log evaluation of gas content from Jiaoshiba shale gas reservoir in Fuling gas field.” Well-logging

Technology, 39(3): 357-362.
Sun, D., and R. Chu. 1994. “A theoretical and experimental study for saturation exponent, N.” Acta Petrolei Sinica, 4: 66-72.
Sun, F., J. Sun, X. Zeng, W. Yuan, J. Zhang, W. Yan, and W. Yan. 2022. “Analysis of the influencing factors on electrical properties and evaluation of gas saturation in marine shales: A case study of the Wufeng-Longmaxi formation in Sichuan Basin.” Frontiers in Earth Science, 10: 824352.
Sun, J., J. Wu, D. Yu, and X. Xu. 2006. “Influential factors in Archie parameters experiment.” Petroleum Geology and Oilfield Development in Daqing, 25(2): 39-41.
Sun, J., H. Dong, M. Arif, L. Yu, Y. Zhang, N. Golsanami, and W. Yan. 2021. “Influence of pore structural properties on gas hydrate saturation and permeability: A coupled pore-scale modelling and X-ray computed tomography method.” Journal of Natural Gas Science and Engineering, 88: 103805.
Sun, Y., B. Bai, and M. Wei. 2015. “Microfracture and surfactant impact on linear cocurrent brine imbibition in gas-saturated shale.” Energy and Fuels, 29(3): 1438-1446.
Sun, Z., Z. He, F. Wang, Y. Han, S. He, Y. Hou, J. Luo, Y. Zheng, and S. Wu. 2022. “Occurrence characteristics of saline-lacustrine shale-oil in the Qianjiang depression, Jianghan Basin, Central China.” Journal of Earth Science, 33(4): 945-962.
Tan, W., R. Lafferty, T. J. Neville. 2014. “Solving complex dual-water equation using Dielectric-NMR-Spectroscopy and conventional logs.” Petrophysics, 55(1): 14-23.
Wang, G., S. Long, Y. Ju, C. Huang, and Y. Peng. 2018. “Application of horizontal wells in three-dimensional shale reservoir modeling: A case study of Longmaxi-Wufeng shale in Fuling gas field, Sichuan Basin.” AAPG Bulletin, 102(11): 2333-2354.
Wang, Y., S. Xu, F. Hao, Y. Lu, Z. Shu, D. Yan, and Y. Lu. 2019. “Geochemical and petrographic characteristics of Wufeng-Longmaxi shales, Jiaoshiba area, southwest China: Implication for organic matter differential accumulation.” Marine and Petroleum Geology, 102: 138-154.

Wang, Y., X. Li, H. Wang, W. Wu, S. Jiang, B. Chen, J. Shen, and G. Zhou. 2020. "Prediction of organic matter carbonization zones of the Lower Silurian Longmaxi Formation in the Middle-Upper Yangtze region, China." Journal of Natural Gas Geoscience, 5(3): 105-116.

Wang, Z. 2014. "Practice and cognition of shale gas horizontal well fracturing stimulation in Jiaoshiba of Fuling area." Oil and Gas Geology, 35(3): 425-430.

Wang, Z. 2019. "Reservoir formation conditions and key efficient exploration & development technologies for marine shale gas fields in Fuling area, South China." Acta Petrolei Sinica, 40(3): 370-382.

Wei, Y., X. Liang, and Y. Cao. 2021. "Design and application of high resolution array laterolog tool." World Well-logging Technology, 5: 104-107.

Xia, H., Y. Wang, H. Liu, and S. Yang. 2001. "On enhancing vertical resolution of dual lateral resistivity logs based on ARI logging." Well-logging Technology, 25(2): 114-118.

Xu, L., Z. Liu, Y. Wen, X. Zhou, and F. Luo. 2020. "Shale gas reservoir and gas-bearing properties of middle Niutitang formation in Western Hubei." Special Oil and Gas Reservoirs, 27(4): 1-9.

You, L., X. Wu, Y. Kang, H. Zhang, and X. Yang. 2016. "Non-Archie phenomenon of the tight sandstone's electrical parameters." Progress in Geophysics, 31(5): 2226-2231.

Zeng, X., J. Sun, W. Yan, R. Cui, W. Yuan, W. Yan, and X. Dong. 2020. "New insight into the petrophysical characterization of shales with different fluid saturation states based on nuclear magnetic resonance experiments." Energy & Fuels, 34(5): 5599-5610.

Zhang, J., S. Li, L. Wang, F. Chen, and B. Geng. 2017. "A new method for calculating gas saturation of low-resistivity shale gas reservoirs." Natural Gas Industry, 37(4): 34-41.

Zhang, T., G. S. Ellis, S. C. Ruppel, K. Milliken, and R. Yang. "Effect of organic-matter type and thermal maturity on methane adsorption in shale-gas systems." Organic geochemistry, 47(3): 120-131.

Zhao, P., X. Li, J. Sun, S. Lai, T. Fu, G. Su, and X. Tian. 2014. "Study on mineral composition and brittleness characteristics of shale gas reservoirs from the Lower Paleozoic in the Southern Sichuan Basin." Geoscience, 8: 396-403.

Zhao, S., Y. Yang, J. Zhang, L. Wang, X. Wang, C. Luo, and C. Tian. 2016. "Micro-layers division and fine reservoirs contrast of Lower Silurian Longmaxi Formation shale, Sichuan Basin, SW China." Natural Gas Geoscience, 27(3): 470-487.

Zou, C., Z. Yang, S. Sun, Q. Zhao, W. Bai, H. Liu, S. Pan, S. Wu, and Y. Yuan. 2020a. "Exploring petroleum inside source kitchen: Shale oil and gas in Sichuan Basin." Science China: Earth Sciences, 63(7): 934-953.

Zou, C., S. Pan, Z. Jing, J. Gao, Z. Yang, S. Wu, and Q. Zhao. 2020b. "Shale oil and gas revolution and its impact." Acta Petrolei Sinica, 41(1): 1-12.

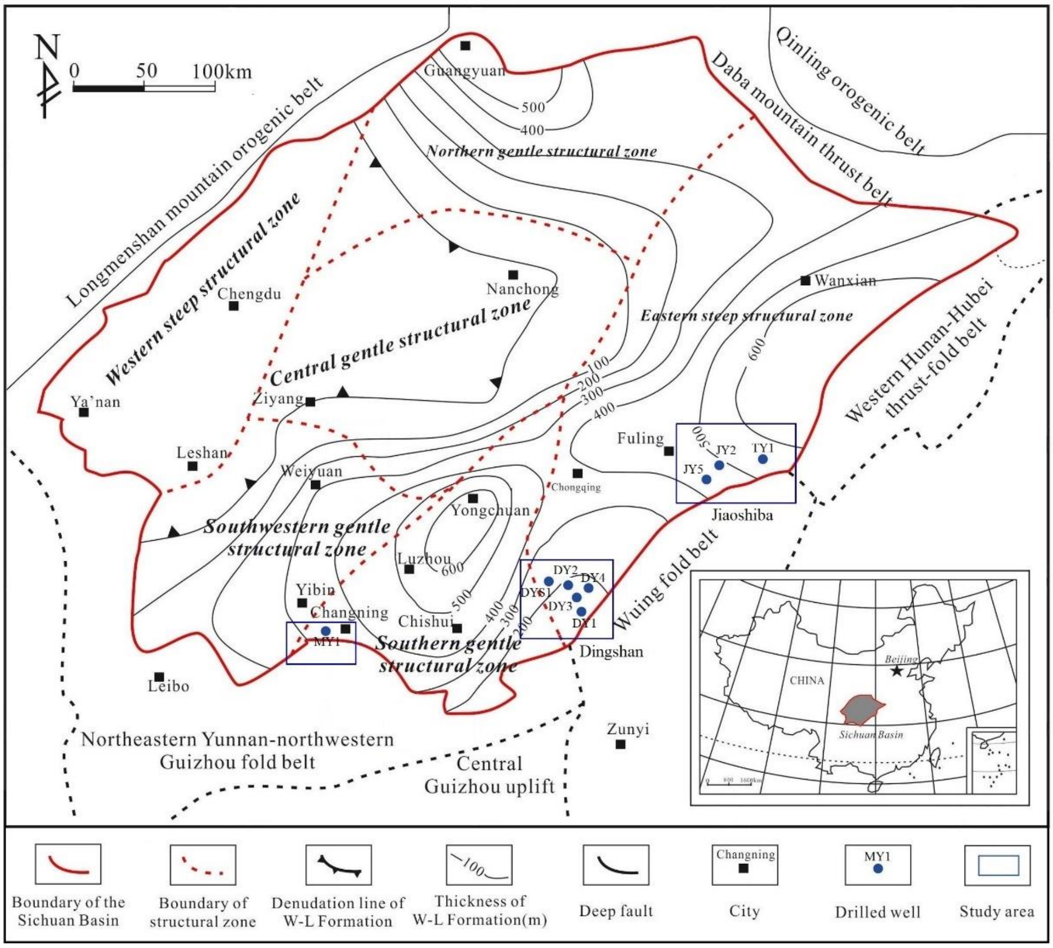

Fig. 1. Regional structural location and well location distribution in the Sichuan Basin, China. This figure was adapted with permission from Chen et al. (2019). Copyright 2019 Elsevier.

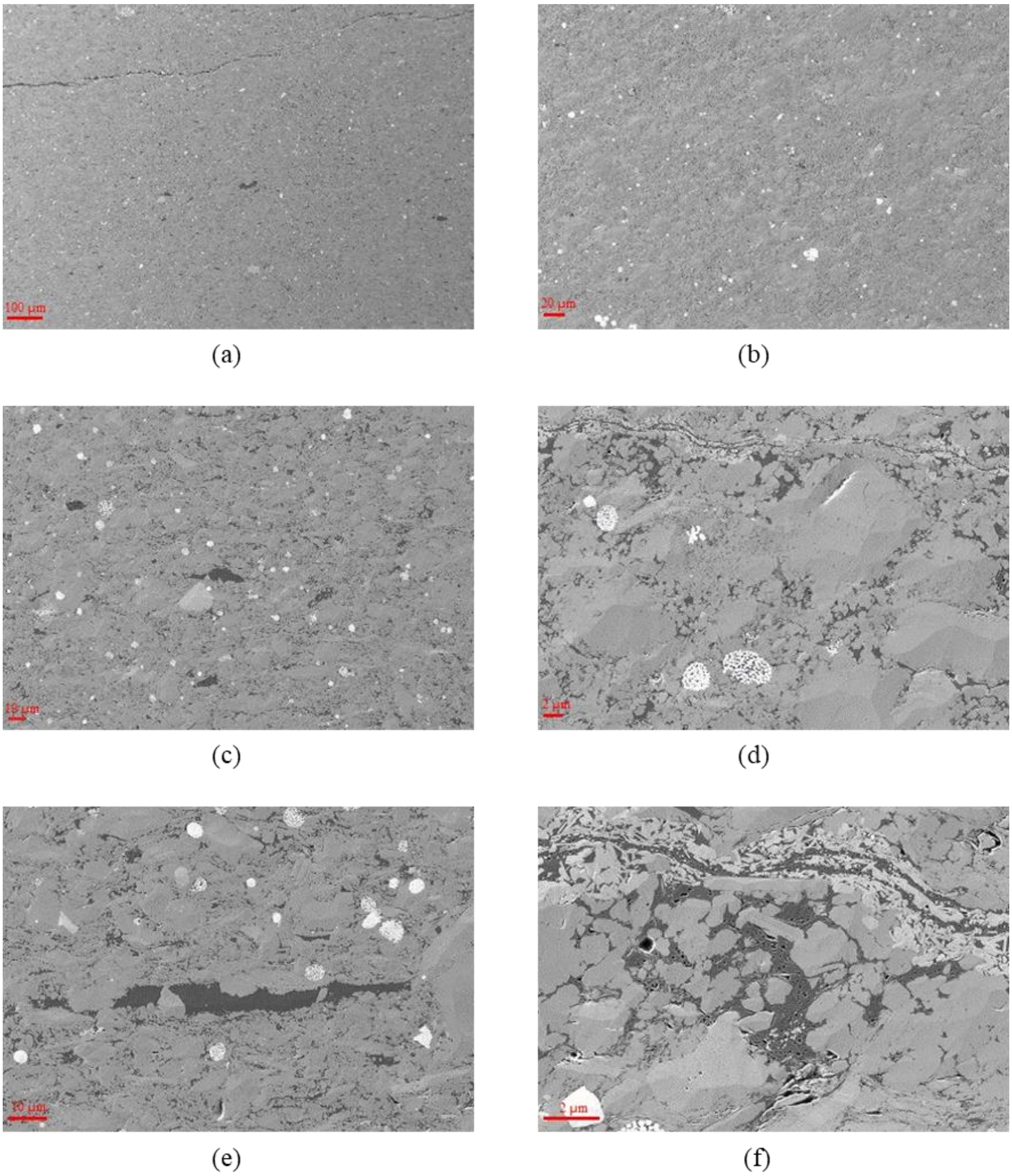

Fig. 2. SEM images of shale in multi-resolution.

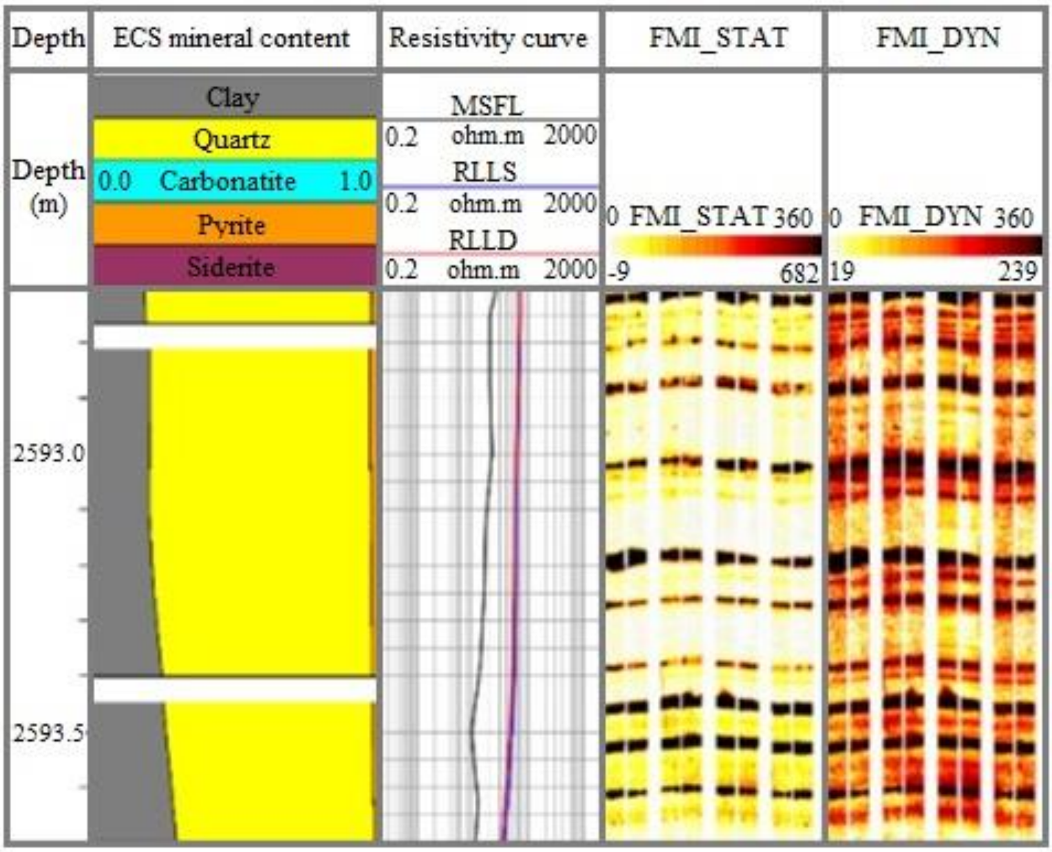

Fig. 3. FMI imaging of low-resistivity thin layer in shale.

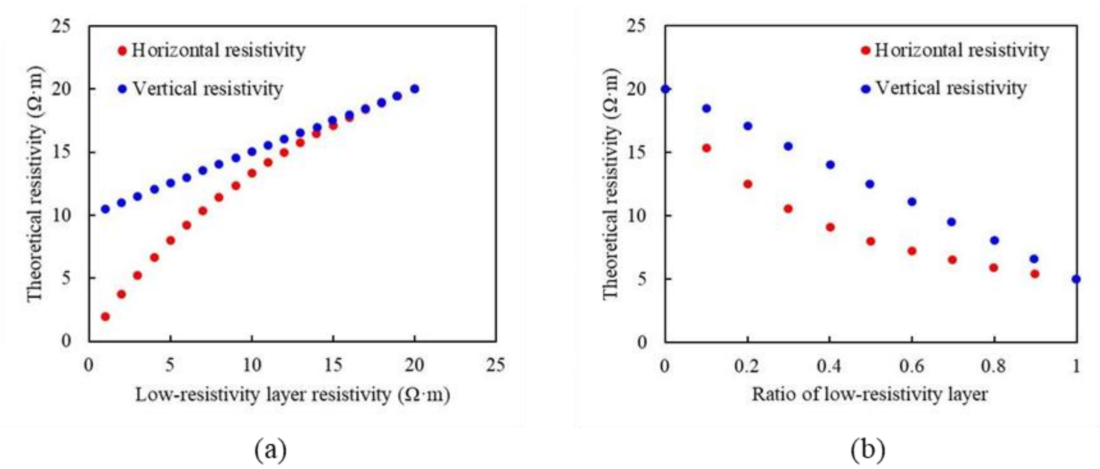

Fig. 4. The variation of horizontal and vertical resistivity with (a) resistivity and (b) the proportion of low-resistivity layer.

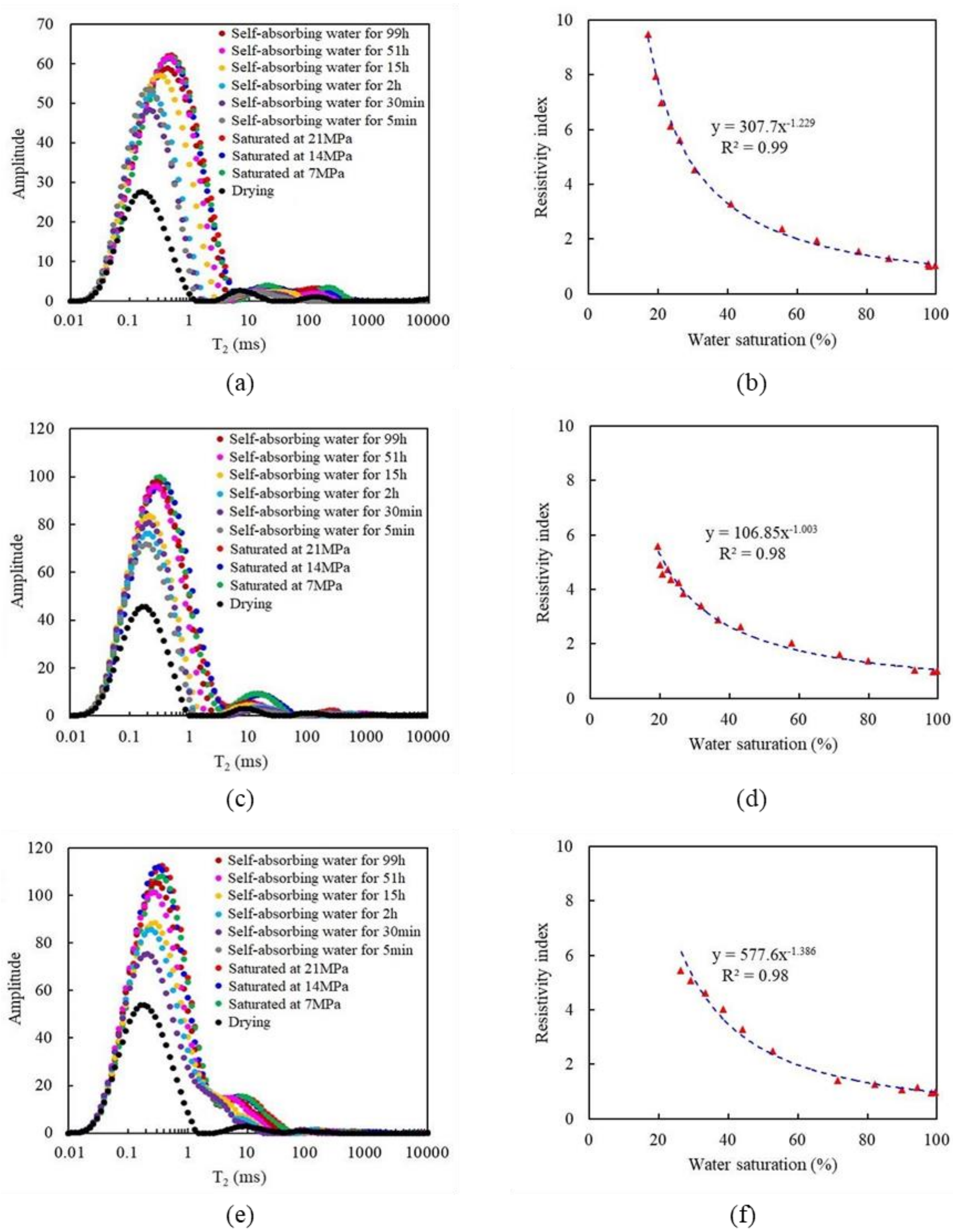

Fig. 5. The variation of NMR T_2 spectrum and resistivity index with water saturation in JY5-2 ((a) and (b)), JY8-3 ((c) and (d)), and DYS1-1 ((e) and (f)).

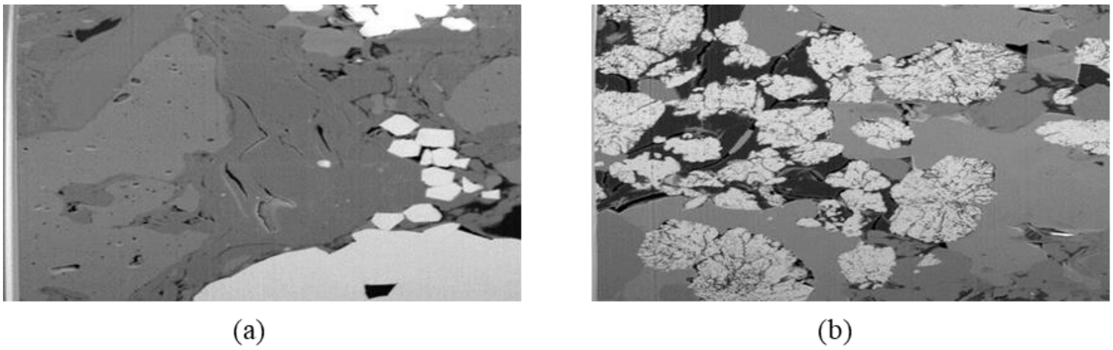

Fig. 6. The FIB-SEM scanning results of shale. (a) DYS1-3, and (b) MY1-2.

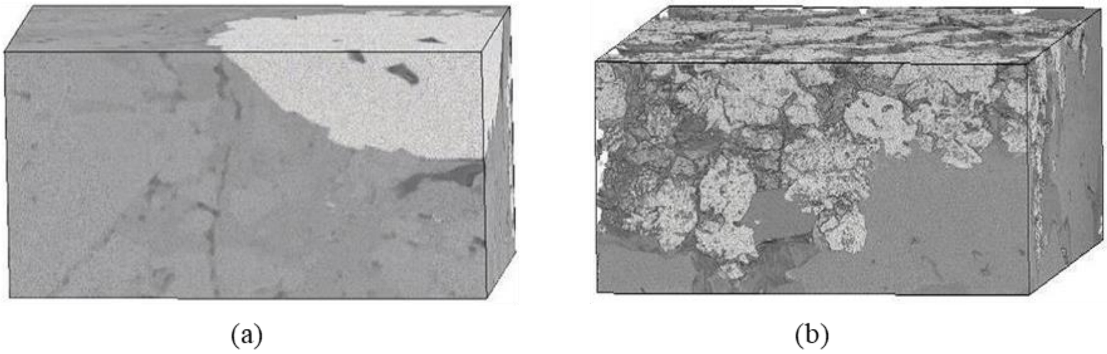

Fig. 7. The 3D digital shale. (a) DYS1-3, and (b) MY1-2.

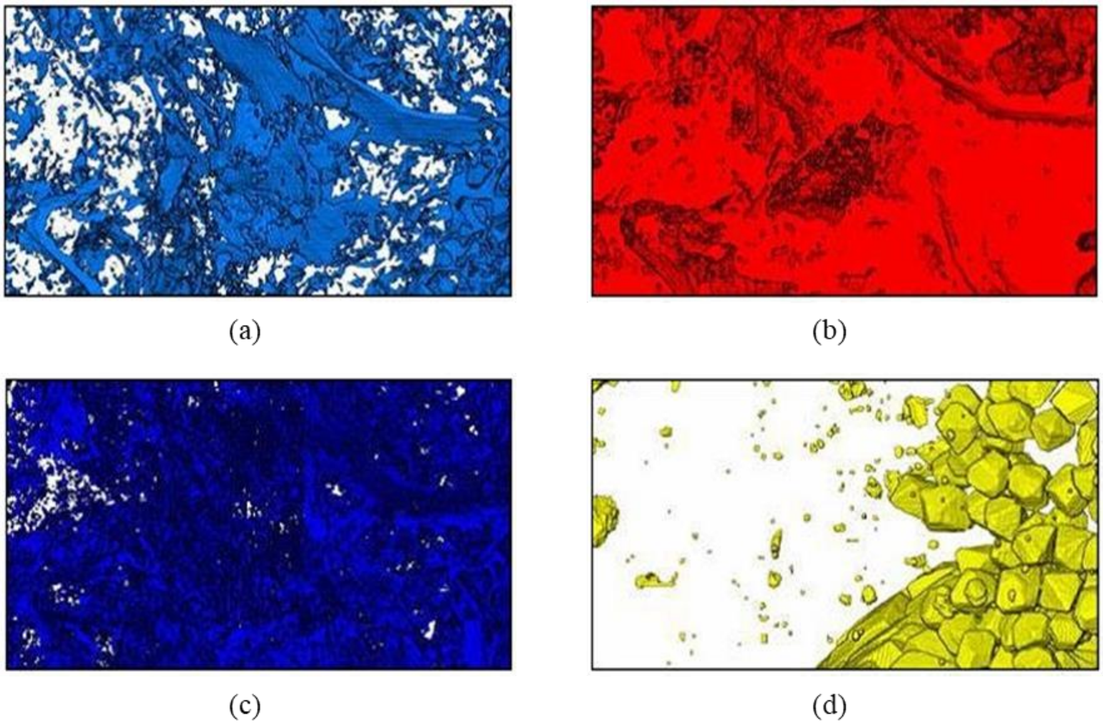

Fig. 8. The components extraction results of digital shale. (a) Pores, (b) clay, (c) organic matter and (d) pyrite.

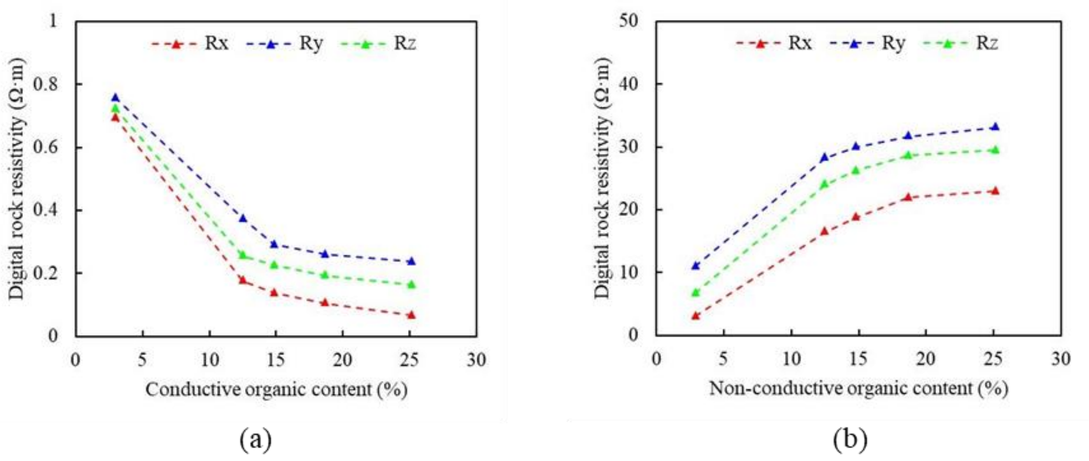

Fig. 9. The influence of organic content on shale resistivity. (a) Conductive organic content and (b) non-conductivity organic content.

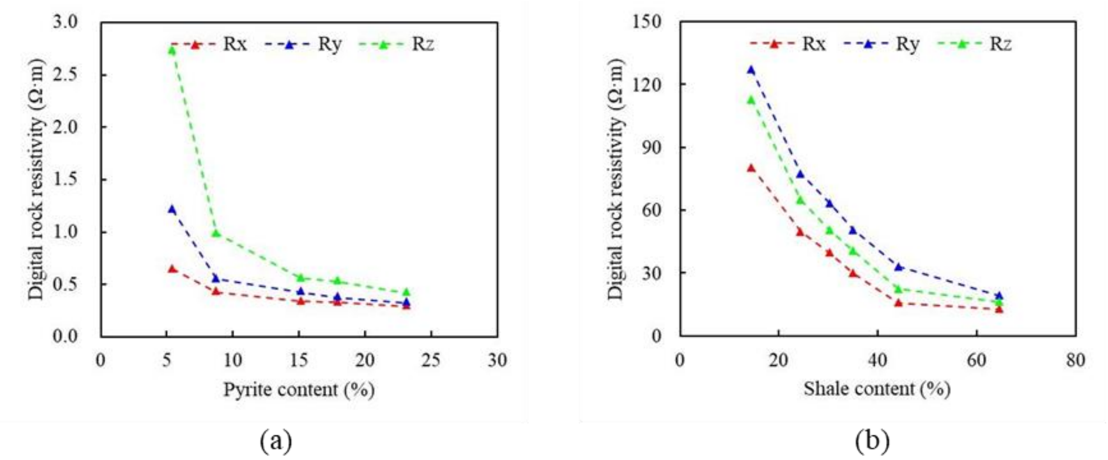

Fig. 10. The influence of mineral composition content on shale resistivity. (a) Pyrite and (b) clay.

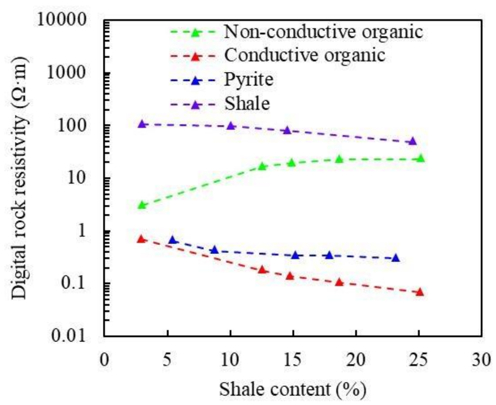

Fig. 11. The influence of different shale component on resistivity.

Table 1. Basic rock parameters of the selected shale samples.

Sample ID	Formation	TOC (%)	Quartz (%)	Feldspar (%)	Calcite (%)	Clay (%)	Pyrite (%)	Helium porosity (%)	Water Porosity (%)	Permeability (mD)
JY2-1	Wufeng	4.45	66.9	8.6	3.4	12.9	8.2	1.64	3.69	0.0015
JY8-3	Wufeng	3.96	34.5	7.6	13.1	44.8	0	1.54	2.17	0.0026
DY2-3	Wufeng	4.77	23.9	3.6	17.5	51.2	3.8	1.41	2.54	0.0032
DY3-5	Wufeng	5.77	76.2	0	8.9	14.9	0	2.65	3.16	0.0013
JY5-2	Longmaxi	2.97	37.5	6.0	19.5	34.4	2.6	1.58	2.64	0.0051
JY5-4	Longmaxi	4.33	36.1	9.1	18.6	32.2	4.0	0.82	3.84	0.0041
JY5-5	Longmaxi	3.94	76.6	1.6	6.8	12.4	2.6	0.92	1.83	0.0416
DY1-2	Longmaxi	2.53	44.0	5.0	10.0	38.0	3.0	1.29	1.64	0.0555
DY3-1	Longmaxi	1.19	34.3	5.9	3.7	56.1	0	1.54	2.68	0.0056
DY4-2	Longmaxi	4.78	51.4	4.9	11.2	29.0	3.5	1.93	3.81	0.0003
DYS1-1	Longmaxi	1.85	32.5	5.5	5.4	51.9	2.3	2.51	3.08	0.2390
DYS1-3	Longmaxi	2.89	40.3	3.4	12.1	36.7	5.8	3.51	4.62	0.9940
TY1-1	Longmaxi	1.97	35.2	8.9	25.8	27.1	3.0	0.33	2.22	0.0001
MY1-2	Longmaxi	6.59	39.0	0	33.3	24.5	3.2	0.37	1.45	0.0002